A Molecular Photoelectrode for Water Oxidation Inspired by Photosystem II

Degao Wang[1#], Renato N. Sampaio[1#], Ludovic Troian-Gautier,[1] Seth L. Marquard,[1] Byron H. Farnum,[2] Benjamin D. Sherman,[3] Matthew V. Sheridan,[1] Christopher J. Dares,[4] Gerald J. Meyer, [1] Thomas J. Meyer[1*]

[1]Department of Chemistry, University of North Carolina at Chapel Hill, Chapel Hill, North Carolina 27599-3290, USA.

[2] Department of Chemistry and Biochemistry, Auburn University, Auburn, Alabama 36849, USA.

[3] Department of Chemistry, Texas Christian University, Fort Worth, Texas 76129, United States

[4]Department of Chemistry and Biochemistry, Florida International University, 11200 SW 8th St, Miami, Florida 33199, USA.

[#]D.W. and R.N.S. contributed equally to this work.

Abstract: In artificial photosynthesis, the sun drives water splitting into H_2 and O_2 or converts CO_2 into a useful form of carbon. In most schemes, water oxidation is typically the limiting half-reaction. Here, we introduce a molecular approach to the design of a photoanode that incorporates an electron acceptor, a sensitizer, an electron donor, and a water oxidation catalyst in a single molecular assembly. The strategy mimics the key elements in Photosystem II by initiating light-driven water oxidation with integration of a light absorber, an electron acceptor, an electron donor, and a catalyst in a controlled molecular environment on the surface of a conducting oxide electrode. Visible excitation of the assembly results in the appearance of reductive equivalents at the electrode and oxidative equivalents at a catalyst on the surface that persist for seconds in aqueous solutions. Steady-state illumination of the assembly with 440 nm light with an applied bias results in photoelectrochemical water oxidation with a per-photon absorbed efficiency of 2.3%. The results are notable in demonstrating that light-driven water oxidation can be carried out at a conductive electrode in a structure with the functional elements of Photosystem II including charge separation and water oxidation.

Introduction

Generating high-energy fuels with sunlight is a central goal of artificial photosynthesis.[1-4] Pioneering work by Fujishima and Honda showed that direct band gap excitation of a semiconductor (TiO_2) with a Pt cathode provided a basis for water splitting into O_2 and H_2. Progress in this area has continued with the development of modified semiconductor surfaces where the physical and chemical steps required for artificial photosynthesis occur, either within, or on the surface including light absorption, separation of redox equivalents, charge transport, and catalysis.[5-9]

In a parallel effort, molecular donor–chromophore–acceptor assemblies have been developed that absorb visible light and convert solar energy into physically separated, transiently stable, redox-separated states that mimic the components in photosynthesis.[10-12] Research efforts in this area have led to the use of structural models that mimic the important cofactors involved in photosynthesis with the key components shown in **Scheme 1.**[13-15] The models have been useful in mimicking the photophysical behavior of photosynthesis including light capture, energy transfer, and long-range electron transfer. Carrying out efficient photo-catalysis, specifically water splitting into hydrogen and oxygen, has proven more challenging.

Progress in the area has included the development of dye-sensitized photoelectrosynthesis cells (DSPEC) that utilize two photoelectrodes.[16-20] The key elements in the photoelectrode are a molecular dye for light absorption, molecular catalysts, for water oxidation and CO_2 or proton reduction, anchored to mesoporous thin films comprised of semiconductor nanocrystallites.[21-26] In this approach, each component can be investigated separately, maximized in performance, and integrated into an appropriate surface structure.[15, 27-32]

We describe here a surface molecular architecture that provides the functional elements of Photosystem II (PSII) for making O_2. The preparation of the assembly utilizes a stepwise, molecular building block approach with self-assembled, layer-by-layer structures formed on optically transparent, mesoporous conductive electrodes.[15, 33-35] The surface of the electrode incorporates an electron acceptor, a visible light absorber, an electron transfer donor, and a water oxidation catalyst. Each is linked in the underlying structure by Zr(IV) phosphonate bridges. The layer-by-layer strategy avoids complicated synthetic strategies that are typically required to produce covalently linked, donor-sensitizer-acceptor assemblies.[32, 35-37]

The structure of the photoanode is shown in **Scheme 1**. It consists of a mesoporous, conductive indium tin oxide electrode (*nano*ITO), a methyl viologen electron acceptor, [(4,4'-bipyridine, N,N'-dipropylphosphonic acid)] (**MV^{2+}**), a ruthenium(II) polypyridyl complex as a sensitizer, [Ru^{II}(2,2'-bipyridine)(2,2'-bipyridine-4,4'-phosphonic acid)$_2$](Cl)$_2$ (**S**), an iron(II) terpyridyl complex as an electron donor, [Fe^{II}(2,2',2''-terpyridyl-4-phosphonic acid)](Cl)$_2$ (**Fe^{II}**), and a ruthenium(II)-based complex as the water oxidation catalyst, [Ru^{II}(2,2'-bipyridine-6,6'-carboxylic acid)((3-(pyridine-4-yloxy)propyl)phosphonic acid)$_2$)] (**Ru^{II}**). They provide the elements in a final assembly, ***nano*ITO|-MV^{2+}-S-Fe^{II}-Ru^{II}**, which is shown in **Scheme 1** or, as discussed below, in a modified version with an active dimeric catalyst.

In Photosystem II (PSII), the key components are the P680 primary donor, a pheophytin primary acceptor with plastoquinone (Q_A) as the final acceptor, a redox active tyrosine, which acts as an intervening redox storage site, and the $CaMn_4$ oxygen evolving complex (OEC) for water oxidation.[38] Reduced plastoquinone transports electrons away from the protein complex into the thylakoid membrane for transfer of reductive equivalents to a second photosystem in the carbon reduction cycle. Oxidative equivalents are transferred through tyrosine to OEC.[39-42] The photoanode utilizes a vectorial, light-induced free energy gradient that drives oxidative equivalents toward the catalyst.

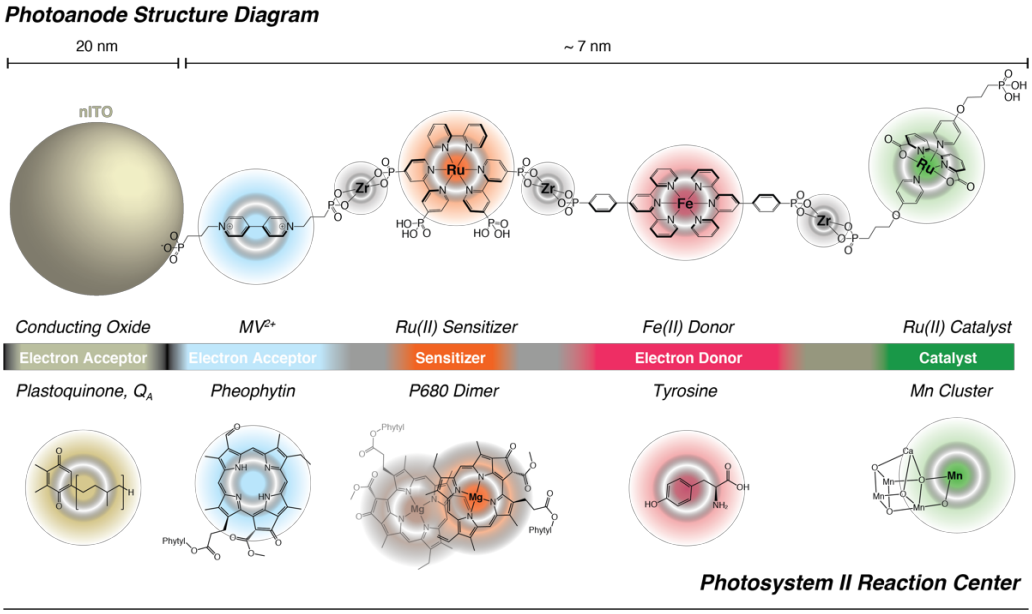

Scheme 1. Structure of the molecular assembly**, *nano*ITO|-MV^{2+}-S-Fe^{II}-Ru^{II}** and a diagram showing the key functional components of PS II.

Results and Discussion

The initial assembly, ***nano*ITO|-MV^{2+}-S-Fe^{II}-Ru^{II}**, was prepared on the surface of 2.3 μm thick mesoporous films composed of indium doped tin oxide nanocrystals (*nano*ITO, 20 nm in diameter). The idealized architecture of the final photoelectrode assembly is illustrated in **Scheme 1**. The visible absorption spectra of each individual component in the assembly is shown in **Figure 1A**. During the layer-by-layer preparation of the photoelectrode, absorption spectra were monitored after the addition of each molecular component, **Figure 1B**. The total surface loadings of the sensitizers, $\Gamma(S) \sim 6.0 \times 10^{-8}$ mol cm^{-2}, were calculated based on the metal-to-ligand charge transfer (MLCT) absorption maximum for Ru(II) at 465 nm with ε =16,400 M^{-1} cm^{-1}. Based on results obtained for previous assemblies,[33] surface loading was consistent with monolayer coverages by the Ru(II) sensitizer. Spectral simulation (**Figure 1B**) revealed that the 1:1:1 assemblies were comprised of a sensitizer (S), electron donor (Fe^{II}), and a water oxidation catalyst (Ru^{II}), on the photoelectrode surface. The structure shown in **Scheme 1** is idealized since the ruthenium sensitizer could potentially be linked to more than one MV^{2+} subunit. The one-to-one stoichiometry of S to Fe^{II}, no doubt arises from steric constraints that inhibit coordination of two iron complexes. The separation distance between the surface and the catalyst center was estimated to be ~70 Å, based on the dimensions of the molecular components. It is worth noting that mesoscopic pore volumes within the *nano*ITO films have average pore diameters of ~360 Å with sufficient internal volume for the formation of the assemblies.[33]

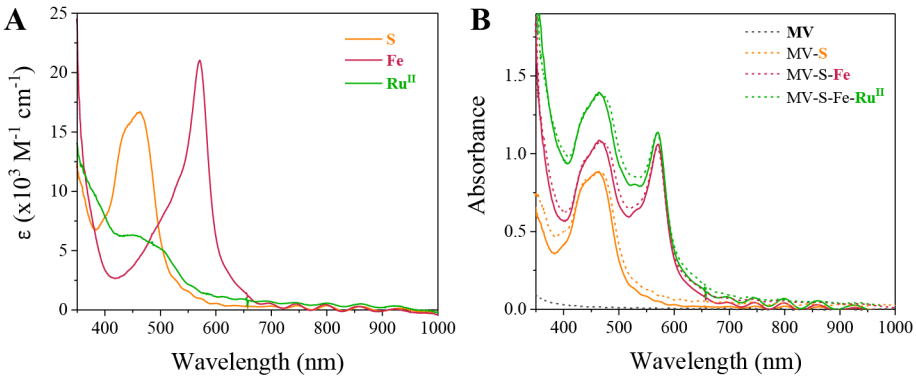

Figure 1: Absorption spectra for individual and mixed component assemblies. Visible absorption spectra for the individual **S**, **Fe^{2+}**, and **Ru^{II}** components anchored on mesoporous ***nano*ITO** (A) and spectra of layer-by-layer combinations (B) (dotted lines). Overlaid on the

experimental data of (B) are simulated spectra (solid lines) for equimolar additions of the spectra shown in (A).

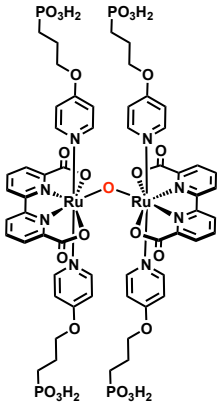

Scheme 2: A dimeric structure of the μ-oxo catalyst, $\mathbf{Ru^{III}ORu^{III}}$, which is the active species in the actual assemblies.

The redox properties of the photoelectrode and its components were quantified by spectro-electrochemical measurements, **Figure 2**, by monitoring absorption spectral changes following stepwise application of positive or negative potentials. Gradually decreasing the applied potential, E_{app}, from 0 to −0.4 V resulted in the reduction of MV^{2+} to MV^{+} with a spectral maximum appearing at 600 nm for MV^{+} (**Figure S1**). Oxidation of the sensitizer **S** ($E_{1/2}$ = 1.35 V vs NHE) and of the $\mathbf{Fe^{II}}$ ($E_{1/2}$ = 1.14 V vs NHE) donor resulted in the reversible loss of the characteristic MLCT bands with isosbestic points maintained between the oxidized and reduced forms. Absorption spectra measured before and after oxidation of the catalyst as $\mathbf{Ru^{II}}$ are shown in **Figure 2C**. The latter is complicated by the formation of the μ-oxo-bridged catalyst dimer $\mathbf{Ru^{III}ORu^{III}}$, **Scheme 2**, which occurs following oxidation to Ru^{III} and appears as a characteristically strong absorption feature at 690 nm (**Figure 2C**).[43]

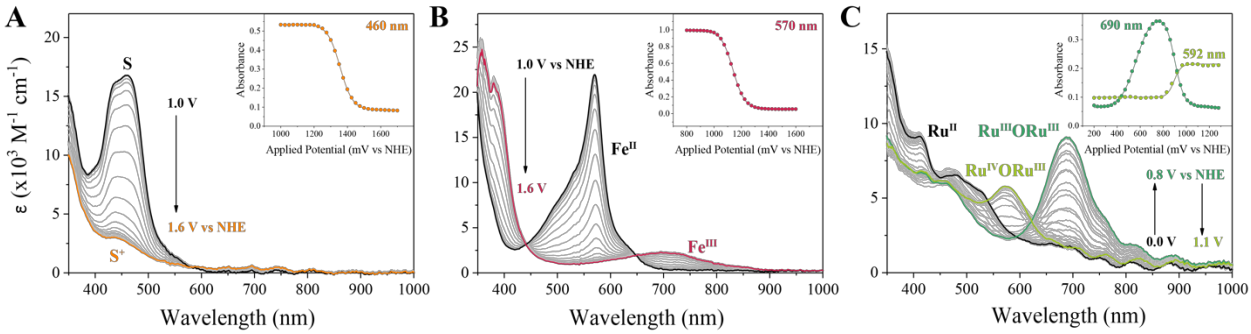

Figure 2. Absorption spectra measured during electrolysis of the individual components within the assembly ***nano*ITO|-MV^{2+}-S-Fe^{II}-Ru^{II}** with spectra of: A) ***nano*ITO|-S** and its oxidation to **-S^{+}**, B) **-Fe^{II}** oxidation to **-Fe^{III}**, and C) oxidation of **-Ru^{II}** to **-Ru^{III}** followed by its dimerization to **Ru^{III}ORu^{III}** (green). The insets show absorbances at key wavelengths as a function of applied potential for the oxidation to **Ru^{III}ORu^{III}** and **Ru^{IV}ORu^{III}** (data in green), with the latter absorbing at 560 nm. The corresponding reduction potentials were obtained by using a modified Nernstian equation.[44] All measurements were performed in 0.1 M acetate buffer (pH 4.65) with 0.5 M $NaClO_4$ as the supporting electrolyte.

Electrochemical oxidation of the dimeric catalyst gives **Ru^{III}ORu^{III}** with $E_{1/2}$ = 0.9 V vs NHE for the **Ru^{IV}ORu^{III}/Ru^{III}ORu^{III}** couple which has a visible absorption band centered at 560 nm. The latter undergoes further oxidation to **Ru^{IV}ORu^{IV}** at a potential around 1.2 V vs NHE and initiates water oxidation (**Figure S2**).

Transient Absorption. The assembly and its individual components were investigated by nanosecond transient absorption measurements at pH 4.65 in 0.1 M acetate buffer, 0.5 M in $NaClO_4$ at room temperature with 488 nm light excitation (**Figure 3**). Excitation of the sensitizer in ***nano*ITO|-S**, led to rapid excited-state injection and back electron transfer, ***nano*ITO(e^{-})|-S^{+} → *nano*ITO|-S**, with k = 6.8 x 10^6 s^{-1}. For the assembly, ***nano*ITO|-MV^{2+}-S**, pulsed light excitation resulted in the initial appearance of a MLCT bleach at 460 nm, with overlapping contributions from excited-state and oxidized S^{+} spectral features. The residual presence of the excited state was also shown by photoluminescence, **Figure 3A**, as a negative signal at ~650 nm. Electron transfer from the excited state, **-S***, through the intervening **-MV^{2+}-** bridge, was rapid with no evidence for the appearance of **–MV$^{\bullet+}$–**. The electron injection efficiency for ***nano*ITO|-MV^{2+}-S** was ϕ_{inj} = 0.19, based on comparative actinometry measurements.[45]

The introduction of the MV^{2+} monolayer between the *nano*ITO surface and the sensitizer **S** significantly increased the charge separation lifetime, ***nano*ITO(e^-)|-MV^{2+}-S^+ → *nano*ITO|-MV^{2+}-S**, with, $k \sim 3 \times 10^3\ s^{-1}$. Excitation of ***nano*ITO|-MV^{2+}-S-Fe^{II}** resulted in instrument response limited injection and quantitative oxidation to Fe^{III} ($\phi = 94.5\%$). The ***nano*ITO(e^-)|-MV^{2+}-S-Fe^{III}** state that resulted, underwent back-electron transfer with $k \sim 6 \times 10^3\ s^{-1}$. In the absence of the **-MV^{2+}-** spacer, in ***nano*ITO|-S-Fe^{II}**, excitation of **-S-** resulted in rapid oxidation of **-Fe^{II}**, to ***nano*ITO(e^-)|-S-Fe^{III}** with back electron transfer with $k \sim 2.6 \times 10^4\ s^{-1}$. Photoluminescence and lifetime measurements on the sensitizer, **S**, were used to estimate the yields of excited-state quenching by the other assembly components, on ZrO_2 (**Figure S3** and **TableS1**).

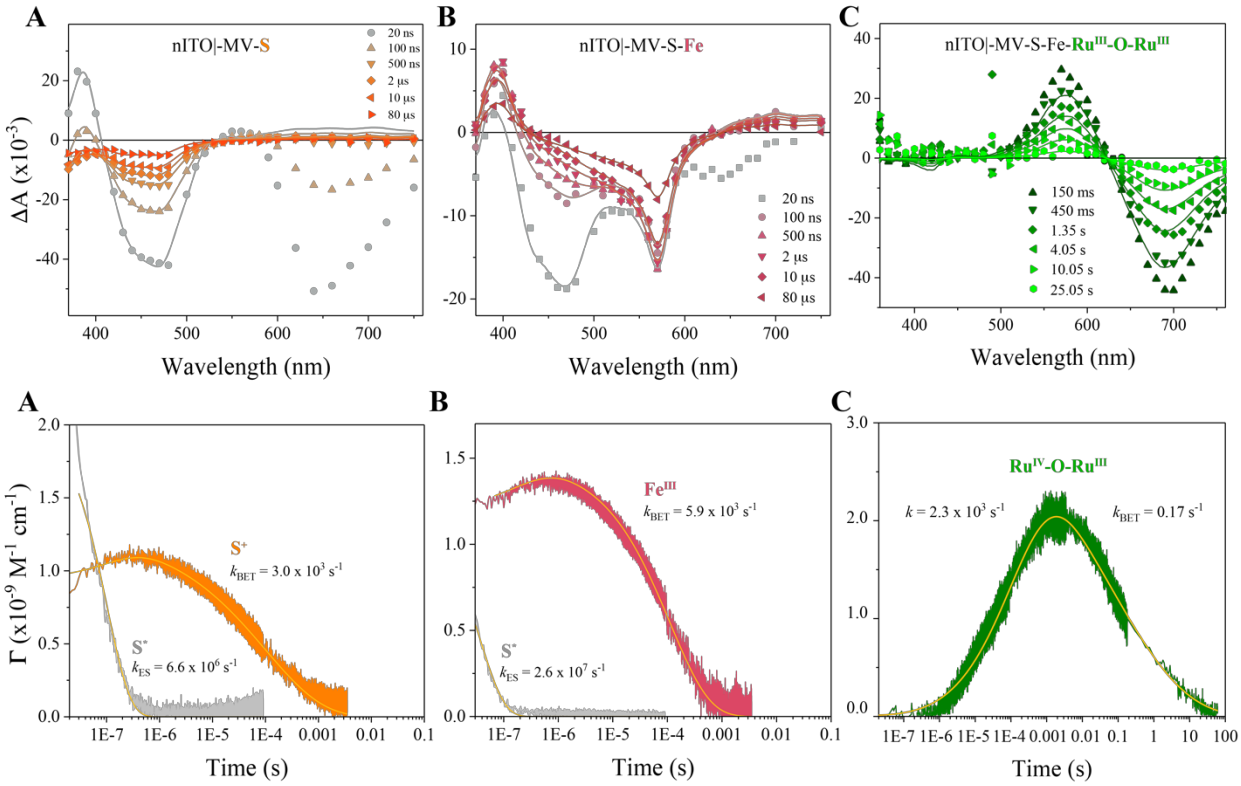

Figure 3. (Top)Transient absorption difference spectra measured at indicated delay times after pulsed 488 nm excitation (8 mJ/cm^2) of: A) ***nano*ITO|-MV^{2+}-S**, B) ***nano*ITO|-MV^{2+}-S-Fe^{II}**, and C) ***nano*ITO|-MV^{2+}-S-Fe^{II}-($Ru^{III}ORu^{III}$)**. Spectral simulations are based on the spectra in **Figures 1** and **2**. Excited-state absorption spectra are also shown. The negative features at wavelengths greater than 600 nm in A) and B) are from sensitizer photoluminescence. (Bottom) Time dependent concentrations of the intermediates with overlaid kinetic fits. All experiments were performed in 0.1 M acetate buffer (pH 4.65) solutions, 0.5 M in $NaClO_4$ as the supporting

electrolyte, under an applied bias of 0.5 V vs NHE at room temperature. (Bottom) Time dependent concentrations of the intermediates obtained by kinetic modeling of the transient data based on the reference spectra shown in Figure 2. Overlaid on the experimental data are kinetic fits from which the rate constants were obtained.

As noted above, although the photoelectrode was assembled in the monomeric form of the Ru^{II}-catalyst, the transient bleach signal at 690 nm in **Figure 3C** shows that the assembly was present initially as ***nano*ITO|-MV^{2+}-S–Fe^{II}-(Ru^{III}ORu^{III})**. Nanosecond excitation at 488 nm was followed by loss of the absorption feature at 700 nm by **Ru^{III}ORu^{III}** with the appearance of **Ru^{IV}ORu^{III}** at 560 nm. The time-dependent results were consistent with light-induced electron transfer to the electrode, ***nano*ITO|-MV^{2+}-S–Fe^{II}-(Ru^{III}ORu^{III})** + hν → ***nano*ITO(e$^-$)|MV^{2+}-S–Fe^{II}-(Ru^{IV}ORu^{III})** followed by back electron transfer. Based on the lifetime data, the rate constant for back-electron transfer from ***nano*ITO(e$^-$)|MV^{2+}-S–Fe^{II}-(Ru^{IV}ORu^{III})** to the electrode was remarkably slow, with $\tau_{BET} \sim 6\ s$, at pH 4.65 in a 0.1 M acetate buffer in 0.5 M $NaClO_4$ at an applied potential of 0.5 V vs. NHE.

A redox potential diagram for the photoelectrode is shown in **Scheme 2**. Based on the redox potentials for the assembly couples, excitation of the sensitizer at λ_{max} = 460 nm results in electron transfer to the electrode by initial electron transfer through the **–MV$^{2+/\bullet+}$-** couple. The initial quenching event is followed by electron transfer from **-Fe^{II}-** to the oxidized sensitizer which is favored by $\Delta G° = -0.21$ V. Based on the excited-state injection yield, and analysis of the transient absorption data in **Figure 3**, the overall yield of separated redox equivalents was 20%. Once formed, **-Fe^{III}-** activates the catalyst, ultimately generating the active form of the catalyst for water oxidation, **Ru^{IV}ORu^{IV}**, after three assembly excitation events.

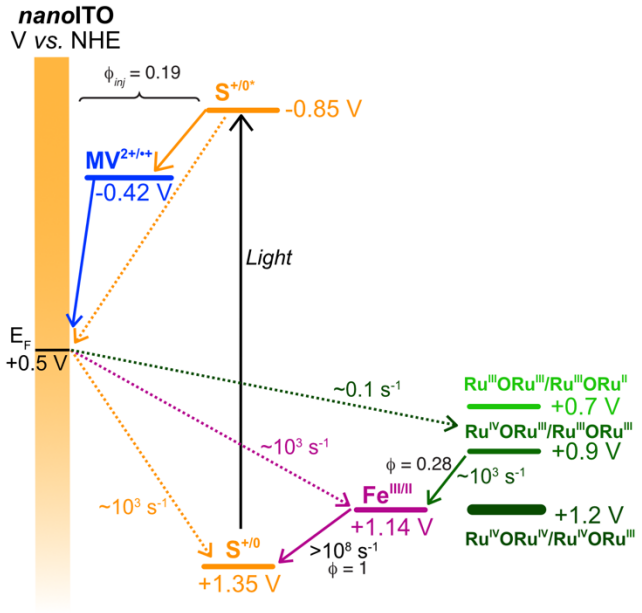

Scheme 2. Redox potential level diagram for ***nano*ITO|-MV^{2+}-S-Fe^{II}-(Ru^{III}ORu^{III})** illustrating the sequence of events that occur following excitation of the sensitizer **S** including electron transfer to the electrode through **–MV^{2+}–**, intermediate redox potential storage in the **-Fe$^{III/II}$** couple, and stepwise oxidation of the catalyst from **Ru^{III}ORu^{III}** to **Ru^{IV}ORu^{IV}** at an external applied potential, E_F, of 0.5 V. Where available, redox potentials and lifetimes are shown for the individual steps.

Water Oxidation. The electrode was utilized in a standard three-electrode photoelectrochemical cell with 1 Sun illumination (100 mW/cm^2, 400 nm filter cut off) at pH 4.65 in an acetate buffer (0.1M) in 0.5 M $NaClO_4$. A platinum wire was used as the counter electrode with a Ag/AgCl reference electrode (0.20 V vs NHE) and a bias of 0.5 V vs. NHE applied to maximize the current for water oxidation. Based on photocurrent measurements (**Figure 4A**) and dark-light photolysis cycles under one sun illumination (100 mW/cm^2, > 400 nm filter), maximum photocurrents of ~250 μA/cm^2 were obtained for ***nano*ITO|-MV^{2+}-S-Fe^{II}-Ru^{III}ORu^{III}** after 30 seconds of illumination. The appearance of O_2 was quantified by a collector-generator electrode technique, (**Figure 4B**).[46] In the O_2 evolution experiments the photocurrent decreased to 75 μA/cm^2 after 10 minutes of illumination and remained at 50 μA/cm^2 after an hour of irradiation. Over 60-minute illumination periods, the Faradaic efficiency for O_2 production was 67%.

Details concerning water oxidation by the assembly are shown in the comparison in **Figure 4.** It illustrates photocurrents over 10 second irradiation periods for the assemblies, **-S-Ru^{III}ORu^{III}**, **-MV^{2+}-S-Ru^{III}ORu^{III}**, **-S-Fe^{II}-Ru^{III}ORu^{III}**, and **-MV^{2+}-S-Fe^{II}-Ru^{III}ORu^{III}**. Based on the data, the chromophore-catalyst assembly ***nano*ITO|-S-Ru^{III}ORu^{III}** is inefficient at producing stable photocurrents. Introduction of the MV^{2+} spacer enhances performance significantly. In the final assembly, with all components present, there is a two- to three-fold increase in efficiency with added **Fe^{II}**.

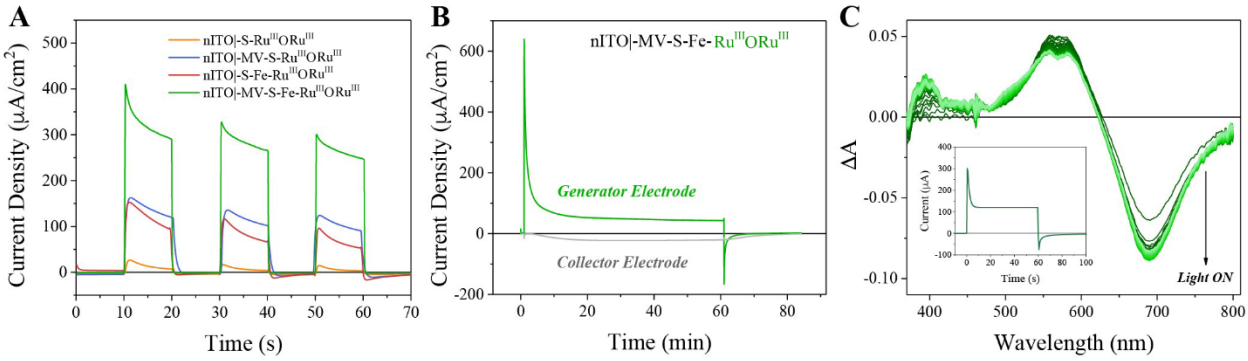

Figure 4. A) Photocurrent measurements for 10 second illumination cycles for the assemblies shown. B) Photocurrent and oxygen evolution measurements for ***nano*ITO|-MV^{2+}-S-Fe^{II}-Ru^{III}ORu^{III}** with a white light source adjusted to 100 mW/cm^2 and a 400 nm cutoff filter. C) Absorption changes and photocurrent densities during monochromatic 450 nm (100 mW/cm^2) steady-state laser excitation illustrating the appearance of the catalyst as **Ru^{IV}ORu^{III}** as the dominant intermediate during water oxidation cycles. All experiments were performed in 0.1 M acetate buffer (pH 4.65) with 0.5 M $NaClO_4$ as the supporting electrolyte, under 0.5 V vs the NHE.

Water oxidation was also investigated by incident photon-to-current efficiency (IPCE) measurements (**Figure S4**). The wavelength dependent photocurrent matches the Ru(II) sensitizer (**S**) absorption spectrum, consistent with it being the important light harvesting component initiating water oxidation. Quantitative analysis of the photolysis data gave a maximum IPCE value of 2.3% at 440 nm after 10 seconds of photolysis (**Figure S4**). Spectrophotometric monitoring, under continuous 450 nm monochromatic irradiation, demonstrated that the dominant form of the catalyst under steady state conditions was **Ru^{IV}ORu^{III} (Figure 4C)**. Comparing these findings with previously reported data for related catalysts suggests an oxidation cycle in which

$Ru^{III}ORu^{III}$ undergoes oxidation to **$Ru^{IV}ORu^{III}$**, followed by oxidation to **$Ru^{IV}ORu^{IV}$**, followed by water oxidation.[43]

Conclusions.

The results described here are a remarkable extension of the phosphonate surface assembly procedure for preparing multiple function assemblies. The target was an assembly that contained the essential elements found in PSII with water oxidation as its objective. The assembly included the essential elements that mimic the key functions in PSII including light absorption, long-range electron transfer, catalysis, and light-induced formation of O_2. In forming the assembly, local spatial control of molecular components led to homogenous, layered structures that contained spatially defined functional elements. Visible excitation of the final assembly results in electron transfer over distances of ~70 Å that form transient intermediates that persist on the seconds timescale and have the ability to carry out water oxidation with visible light on a conductive oxide photoelectrode.

Experimental.

General. All materials and reagents were used as received: Sodium acetate (CH_3COONa, Sigma-Aldrich, ≥ 99%); Sodium perchlorate ($NaClO_4$, Sigma-Aldrich, ≥ 99%); deionized water; fluorine-doped SnO_2 glass (FTO, Hartford Glass Co., Inc. 2.3 mm thick, 15 Ω/cm^2); tin-doped indium oxide nanoparticles (nITO, TC8 DE, Evonik Industries). The transparent conductive nITO thin films were prepared according to previously published methods.[19, 47] Briefly, the *nano*ITO paste was prepared by mixing 0.5g of hydroxypropyl cellulose (MW,100000) into 30% ITO in ethanol solution. After stirring for 2 days, the nanoITO colloidal suspensions were doctor-bladed onto a fluorine-doped tin oxide (FTO) substrate to reach a thickness of approximately 2.5 μm and a width of 1 cm. The substrates were allowed to stand in the dark for 30 minutes prior to being heated at 450°C under a flow of O_2 for 1 hour. The different molecular components were synthesized based on literature procedures.[48-50] UV-visible were performed using an Agilent 8453 UV/visible photodiode array spectrophotometer.

Electrode Preparation. The first step of synthesizing the surface assembly consisted of soaking the *nano*ITO electrodes in 0.1 M $HClO_4$ aqueous solutions containing 2 mM MV^{2+} overnight. After copious rinsing with a 0.1 M $HClO_4$ solution, the derivatized *nano*ITO|-MV^{2+} electrodes

were dried under a flow of N_2 and placed in a 0.1 M Zr^{IV} $HClO_4$ solution. The slides were then immersed in a 0.5 mM ruthenium **S** solution overnight, rinsed with 0.1 M $HClO_4$ solution and dried under an N_2 flow. The slides were then placed in a 0.1 M Zr^{IV} $HClO_4$ solution and then in a 1 mM methanolic solution of $\mathbf{Fe^{II}}$ overnight. After rinsing with methanol, the electrodes were then placed in a 0.1 M Zr^{IV} $HClO_4$ solution and then soaked for 24 hours in a methanol solution containing 3 mM of Ru^{II} to give the complete assembly *nano*ITO|–MV^{2+}-S-Fe^{II}- Ru^{II}.

Electrochemistry. Spectroelectrochemical experiments were performed with an integrated system from Pine Research Instruments.[51] Electrochemical and photoelectrochemical experiments were performed using either a CH Instruments 660D potentiostat or a CH Instruments 760E bipotentiostat. A Thor Labs HPLS 30-04 light source was used to provide white light illumination. For all indicated experiments using 100 mW cm^{-2} white light illumination, the electrochemical cell was positioned an appropriate distance from the light source to receive the indicated light intensity as measured with a photodiode (Newport), and a 400 nm cutoff filter (Newport) was used.

Transient Absorption. Nanosecond transient absorption experiments were conducted on a previously described apparatus.[52] Briefly, the films were inserted at a 45° angle into a standard 1 cm pathlength glass cuvette containing 3mL of an argon purged 0.1M acetate buffer (pH = 4.65, 0.5M $NaClO_4$). A potential of +0.5 V vs NHE was applied to the photoelectrode. A Q-switched, pulsed Nd:YAG laser (Quantel U.S.A. (BigSky) Brilliant B 5-6 ns full width at half-maximum (fwhm), 1 Hz, ~10 mm in diameter) doubled to 532 nm was passed through an OPO and tuned to 488 nm. The laser irradiance at the sample was attenuated to 8 mJ/cm^2. The probe lamp consisted of a 150 W Xenon arc lamp that was often pulsed at 1Hz. Signal detection was achieved using a monochromator (SPEX 1702/04) optically coupled to an R928 photomultiplier tube (Hamamatsu) at a right angle to the excitation laser. Transient data were acquired with a computer-interfaced digital oscilloscope (LeCroy 9450, Dual 330 MHz) with an overall instrument response time of ~10 ns. Injection efficiencies were calculated through actinometric methods as previously reported.[53]

Kinetic data that report on the time dependent concentrations changes (**Figure 3C**, bottom) were obtained by modeling transient data based on a least-square fit that used the spectroelectrochemically generated molar absorptivity spectra shown in **Figure 2**. Recombination kinetics data were nonexponential, but well-described by the Kohlrausch-Williams-Watts (KWW)

kinetic function. [33, 52, 54] Injection efficiencies were calculated through actinometric methods as previously reported.[45, 53] The sensitized TiO_2|-RuP photoelectrode, where RuP = [$Ru^{II}(bpy)_2$(4,4'-$(PO_3H_2)_2$-2,2'bipyridine], was immersed in 0.1 M $HClO_4$ aqueous solutions and used as the actinometer with quantum yield for excited-state injection $\phi_{inj} = 1$.

Transient absorption data shown in Figure 3C required laser excitation with repetition rates longer than 0.001 Hz to ensure complete reversibility between multiple laser pulses for signal averaging. Therefore, for transient spectra measurements, a AvaSpec ULS2048 UV-vis diode array spectrophotometer replaced the photomultiplier as the detector.

IPCE measurements. IPCE measurements were performed with a 100 W Xenon lamp (Newport) powered by 300 W Newport power supply (69907) and Newport monochromator 74100. A Polka Dot Beamsplitters (BPD254S-FS) was used. Photocurrent data was taken at 10 nm increments and the light intensity at each wavelength was recorded using a UDT S370 optometer coupled to a UDT detector (56048). A CH Instruments 760D potentiostat was used to record the photocurrent transients and a bias of 0.5 V vs. NHE was used in 0.1 M acetate buffer (pH 4.65) with 0.5 M $NaClO_4$ as the supporting electrolyte. IPCE values were calculated by using the following equation, IPCE=1240×I/ (P× λ) where I is the measured photocurrent, P the incident light intensity and λ is the incident wavelength. Under 440 nm illumination, the photocurrent was 3.82 μA and the power was 4.59 $x10^{-4}$ W.

Acknowledgment.

This research was supported by the Alliance for Molecular PhotoElectrode Design for Solar Fuels (AMPED), an Energy Frontier Research Center (EFRC) funded by the U.S. Department of Energy, Office of Science, Office of Basic Energy Sciences under Award Number DE-SC0001011 and the U.S. Department of Energy (DOE), Office of Basic Energy Sciences under Award No. DE-SC0015739. L. T.-G. acknowledges personal fellowships from the Belgian American Educational Foundation (BAEF) as well as the Bourse d'Excellence Wallonie-Bruxelles (WBI.World) for generous support.

Supplementary Information

Additional spectroelectrochemistry and cyclic voltammetry, Photoluminescence quenching and incident photon-to-current measurements. This material is available free of charge via the Internet at http://pubs.acs.org.

Corresponding Author

* tjmeyer@unc.edu

Competing interests: Authors have no competing interests.

References:

1. Lewis, N. S.; Nocera, D. G., Powering the Planet: Chemical Challenges in Solar Energy Utilization. *Proc. Natl. Acad. Sci. USA* **2006,** *103*, 15729-15735.
2. Meyer, T. J., Chemical Approaches to Artificial Photosynthesis. *Acc. Chem. Res.* **1989,** *22*, 163-170.
3. Meyer, T. J., Oxidizing Water two Ways. *Nature Chem.* **2011,** *3*, 757.
4. Walter, M. G.; Warren, E. L.; McKone, J. R.; Boettcher, S. W.; Mi, Q.; Santori, E. A.; Lewis, N. S., Solar Water Splitting Cells. *Chem. Rev.* **2010,** *110*, 6446-6473.
5. Fujishima, A.; Honda, K., Electrochemical Photolysis of Water at a Semiconductor Electrode. *Nature* **1972,** *238*, 37-38.
6. Hu, S.; Shaner, M. R.; Beardslee, J. A.; Lichterman, M.; Brunschwig, B. S.; Lewis, N. S., Amorphous TiO_2 Coatings Stabilize Si, GaAs, and GaP Photoanodes for Efficient Water Oxidation. *Science* **2014,** *344*, 1005-1009.
7. Kenney, M. J.; Gong, M.; Li, Y.; Wu, J. Z.; Feng, J.; Lanza, M.; Dai, H., High-Performance Silicon Photoanodes Passivated with Ultrathin Nickel Films for Water Oxidation. *Science* **2013,** *342*, 836-840.
8. Liu, C.; Dasgupta, N. P.; Yang, P., Semiconductor Nanowires for Artificial Photosynthesis. *Chem. Mater.* **2014,** *26*, 415-422.
9. Sivula, K.; Le Formal, F.; Grätzel, M., Solar Water Splitting: Progress Using Hematite (α-Fe_2O_3) Photoelectrodes. *ChemSusChem* **2011,** *4*, 432-449.
10. Imahori, H.; Norieda, H.; Yamada, H.; Nishimura, Y.; Yamazaki, I.; Sakata, Y.; Fukuzumi, S., Light-Harvesting and Photocurrent Generation by Gold Electrodes Modified with Mixed Self-Assembled Monolayers of Boron−Dipyrrin and Ferrocene−Porphyrin−Fullerene Triad. *J. Am. Chem. Soc.* **2001,** *123*, 100-110.
11. Seta, P.; Bienvenue, E.; Moore, A. L.; Mathis, P.; Bensasson, R. V.; Liddell, P.; Pessiki, P. J.; Joy, A.; Moore, T. A.; Gust, D., Photodriven Transmembrane Charge Separation and Electron Transfer by a Carotenoporphyrin–Quinone Triad. *Nature* **1985,** *316*, 653-655.
12. Sherman, B. D.; Vaughn, M. D.; Bergkamp, J. J.; Gust, D.; Moore, A. L.; Moore, T. A., Evolution of Reaction Center Mimics to Systems Capable of Generating Solar Fuel. *Photosynthesis Research* **2014,** *120*, 59-70.
13. Imahori, H.; Hagiwara, K.; Aoki, M.; Akiyama, T.; Taniguchi, S.; Okada, T.; Shirakawa, M.; Sakata, Y., Linkage and Solvent Dependence of Photoinduced Electron Transfer in Zincporphyrin-C_{60} Dyads. *J. Am. Chem. Soc.* **1996,** *118*, 11771-11782.
14. Liddell, P. A.; Kuciauskas, D.; Sumida, J. P.; Nash, B.; Nguyen, D.; Moore, A. L.; Moore, T. A.; Gust, D., Photoinduced Charge Separation and Charge Recombination to a Triplet State in a Carotene−Porphyrin−Fullerene Triad. *J. Am. Chem. Soc.* **1997,** *119*, 1400-1405.

15. Sampaio, R. N.; Troian-Gautier, L.; Meyer, G. J., A Charge-Separated State that Lives for Almost a Second at a Conductive Metal Oxide Interface. *Angew. Chem.* **2018,** *130*, 15616-15620.
16. Alibabaei, L.; Sherman, B. D.; Norris, M. R.; Brennaman, M. K.; Meyer, T. J., Visible Photoelectrochemical Water Splitting into H_2 and O_2 in a Dye-Sensitized Photoelectrosynthesis Cell. *Proc. Natl. Acad. Sci. USA* **2015,** *112*, 5899-5902.
17. Li, F.; Fan, K.; Xu, B.; Gabrielsson, E.; Daniel, Q.; Li, L.; Sun, L., Organic Dye-Sensitized Tandem Photoelectrochemical Cell for Light Driven Total Water Splitting. *J. Am. Chem. Soc.* **2015,** *137*, 9153-9159.
18. Moore, G. F.; Blakemore, J. D.; Milot, R. L.; Hull, J. F.; Song, H.-e.; Cai, L.; Schmuttenmaer, C. A.; Crabtree, R. H.; Brudvig, G. W., A Visible Light Water-Splitting Cell with a Photoanode Formed by Codeposition of a High-Potential Porphyrin and an Iridium Water-Oxidation Catalyst. *Energ. Environ. Sci.* **2011,** *4*, 2389-2392.
19. Sherman, B. D.; Sheridan, M. V.; Wee, K.-R.; Marquard, S. L.; Wang, D.; Alibabaei, L.; Ashford, D. L.; Meyer, T. J., A Dye-Sensitized Photoelectrochemical Tandem Cell for Light Driven Hydrogen Production from Water. *J. Am. Chem. Soc.* **2016,** *138*, 16745-16753.
20. Xu, P.; McCool, N. S.; Mallouk, T. E., Water Splitting Dye-Sensitized Solar Cells. *Nano Today* **2017,** *14*, 42-58.
21. Concepcion, J. J.; House, R. L.; Papanikolas, J. M.; Meyer, T. J., Chemical Approaches to Artificial Photosynthesis. *Proc. Natl. Acad. Sci. USA* **2012,** *109*, 15560-15564.
22. Duan, L.; Tong, L.; Xu, Y.; Sun, L., Visible Light-Driven Water Oxidation—From Molecular Catalysts to Photoelectrochemical Cells. *Energ. Environ. Sci.* **2011,** *4*, 3296-3313.
23. Gao, Y.; Ding, X.; Liu, J.; Wang, L.; Lu, Z.; Li, L.; Sun, L., Visible Light Driven Water Splitting in a Molecular Device with Unprecedentedly High Photocurrent Density. *J. Am. Chem. Soc.* **2013,** *135*, 4219-4222.
24. Gust, D.; Moore, T. A.; Moore, A. L., Solar Fuels via Artificial Photosynthesis. *Acc. Chem. Res.* **2009,** *42*, 1890-1898.
25. Youngblood, W. J.; Lee, S.-H. A.; Maeda, K.; Mallouk, T. E., Visible Light Water Splitting Using Dye-Sensitized Oxide Semiconductors. *Acc. Chem. Res.* **2009,** *42*, 1966-1973.
26. Yu, Z.; Li, F.; Sun, L., Recent Advances in Dye-Sensitized Photoelectrochemical Cells for Solar Hydrogen Production Based on Molecular Components. *Energ. Environ. Sci.* **2015,** *8*, 760-775.
27. Shan, B.; Farnum, B. H.; Wee, K.-R.; Meyer, T. J., Generation of Long-Lived Redox Equivalents in Self-Assembled Bilayer Structures on Metal Oxide Electrodes. *J. Phys. Chem. C* **2017,** *121*, 5882-5890.
28. Shan, B.; Sherman, B. D.; Klug, C. M.; Nayak, A.; Marquard, S. L.; Liu, Q.; Bullock, R. M.; Meyer, T. J., Modulating Hole Transport in Multilayered Photocathodes with Derivatized p-Type Nickel Oxide and Molecular Assemblies for Solar-Driven Water Splitting. *J. Phys. Chem. Lett.* **2017,** *8*, 4374-4379.
29. Wang, D.; Marquard, S. L.; Troian-Gautier, L.; Sheridan, M. V.; Sherman, B. D.; Wang, Y.; Eberhart, M. S.; Farnum, B. H.; Dares, C. J.; Meyer, T. J., Interfacial Deposition of Ru(II) Bipyridine-Dicarboxylate Complexes by Ligand Substitution for Applications in Water Oxidation Catalysis. *J. Am. Chem. Soc.* **2018,** *140*, 719-726.
30. Wang, D.; Sheridan, M. V.; Shan, B.; Farnum, B. H.; Marquard, S. L.; Sherman, B. D.; Eberhart, M. S.; Nayak, A.; Dares, C. J.; Das, A. K.; Bullock, R. M.; Meyer, T. J., Layer-by-Layer Molecular Assemblies for Dye-Sensitized Photoelectrosynthesis Cells Prepared by Atomic Layer Deposition. *J. Am. Chem. Soc.* **2017,** *139*, 14518-14525.

31. Wang, D.; Sherman, B. D.; Farnum, B. H.; Sheridan, M. V.; Marquard, S. L.; Eberhart, M. S.; Dares, C. J.; Meyer, T. J., Plasmon-Enhanced Light-Driven Water Oxidation by a Dye-Sensitized Photoanode. *Proc. Natl. Acad. Sci. USA* **2017,** *114*, 9809-9813.
32. Shan, B.; Nayak, A.; N. Sampaio, R.; Eberhart, M. S.; Troian-Gautier, L.; Brennaman, M. K.; Meyer, G. J.; Meyer, T. J., Direct Photoactivation of a Nickel-Based, Water-Reduction Photocathode by a Highly Conjugated Supramolecular Chromophore. *Energ. Environ. Sci.* **2018,** *11*, 447-455.
33. Farnum, B. H.; Wee, K.-R.; Meyer, T. J., Self-Assembled Molecular p/n Junctions for Applications in Dye-Sensitized Solar Energy Conversion. *Nature Chem.* **2016,** *8*, 845.
34. Hanson, K.; Torelli, D. A.; Vannucci, A. K.; Brennaman, M. K.; Luo, H.; Alibabaei, L.; Song, W.; Ashford, D. L.; Norris, M. R.; Glasson, C. R. K.; Concepcion, J. J.; Meyer, T. J., Self-Assembled Bilayer Films of Ruthenium(II)/Polypyridyl Complexes through Layer-by-Layer Deposition on Nanostructured Metal Oxides. *Angew. Chem.* **2012,** *124*, 12954-12957.
35. Wang, J. C.; Hill, S. P.; Dilbeck, T.; Ogunsolu, O. O.; Banerjee, T.; Hanson, K., Multimolecular Assemblies on High Surface Area Metal Oxides and Their Role in Interfacial Energy and Electron Transfer. *Chem. Soc. Rev.* **2018,** *47*, 104-148.
36. Gross, M. A.; Creissen, C. E.; Orchard, K. L.; Reisner, E., Photoelectrochemical Hydrogen Production in Water Using a Layer-by-Layer Assembly of a Ru Dye and Ni Catalyst on NiO. *Chem. Sci.* **2016,** *7*, 5537-5546.
37. Nayak, A.; Knauf, R. R.; Hanson, K.; Alibabaei, L.; Concepcion, J. J.; Ashford, D. L.; Dempsey, J. L.; Meyer, T. J., Synthesis and Photophysical Characterization of Porphyrin and Porphyrin–Ru(II) Polypyridyl Chromophore–Catalyst Assemblies on Mesoporous Metal Oxides. *Chem. Sci.* **2014,** *5*, 3115-3119.
38. Meyer, T. J.; Huynh, M. H. V.; Thorp, H. H., The Possible Role of Proton-Coupled Electron Transfer (PCET) in Water Oxidation by Photosystem II. *Angew. Chem. Int. Ed.* **2007,** *46*, 5284-5304.
39. Hammarström, L.; Styring, S., Proton-Coupled Electron Transfer of Tyrosines in Photosystem II and Model Systems for Artificial Photosynthesis: the Role of a Redox-Active Link Between Catalyst and Photosensitizer. *Energ. Environ. Sci.* **2011,** *4*, 2379-2388.
40. McEvoy, J. P.; Brudvig, G. W., Water-Splitting Chemistry of Photosystem II. *Chem. Rev.* **2006,** *106*, 4455-4483.
41. Megiatto, J. D.; Antoniuk-Pablant, A.; Sherman, B. D.; Kodis, G.; Gervaldo, M.; Moore, T. A.; Moore, A. L.; Gust, D., Mimicking the Electron Transfer Chain in Photosystem II With a Molecular Triad Thermodynamically Capable of Water Oxidation. *Proc. Natl. Acad. Sci. USA* **2012,** *109*, 15578-15583.
42. Zhao, Y.; Swierk, J. R.; Megiatto, J. D.; Sherman, B.; Youngblood, W. J.; Qin, D.; Lentz, D. M.; Moore, A. L.; Moore, T. A.; Gust, D.; Mallouk, T. E., Improving the Efficiency of Water Splitting in Dye-Sensitized Solar Cells by Using a Biomimetic Electron Transfer Mediator. *Proc. Natl. Acad. Sci. USA* **2012,** *109*, 15612-15616.
43. Concepcion, J. J.; Zhong, D. K.; Szalda, D. J.; Muckerman, J. T.; Fujita, E., Mechanism of Water Oxidation by [Ru(bda)(L)2]: the Return of the "Blue Dimer". *Chem. Commun.* **2015,** *51*, 4105-4108.
44. Piechota, E. J.; Troian-Gautier, L.; Sampaio, R. N.; Brennaman, M. K.; Hu, K.; Berlinguette, C. P.; Meyer, G. J., Optical Intramolecular Electron Transfer in Opposite Directions through the Same Bridge That Follows Different Pathways. *J. Am. Chem. Soc.* **2018,** *140*, 7176-7186.

45. Bergeron, B. V.; Kelly, C. A.; Meyer, G. J., Thin Film Actinometers for Transient Absorption Spectroscopy: Applications to Dye-Sensitized Solar Cells. *Langmuir* **2003,** *19*, 8389-8394.
46. Sherman, B. D.; Sheridan, M. V.; Dares, C. J.; Meyer, T. J., Two Electrode Collector–Generator Method for the Detection of Electrochemically or Photoelectrochemically Produced O_2. *Analytical Chemistry* **2016,** *88*, 7076-7082.
47. Liu, F.; Concepcion, J. J.; Jurss, J. W.; Cardolaccia, T.; Templeton, J. L.; Meyer, T. J., Mechanisms of Water Oxidation from the Blue Dimer to Photosystem II. *Inorg. Chem.* **2008,** *47*, 1727-1752.
48. Farnum, B. H.; Wee, K.-R.; Meyer, T. J., Self-Assembled Molecular p/n Junctions for Applications in Dye-Sensitized Solar Energy Conversion. *Nat. Chem.* **2016,** *8*, 845-852.
49. Cummins, D.; Boschloo, G.; Ryan, M.; Corr, D.; Rao, S. N.; Fitzmaurice, D., Ultrafast Electrochromic Windows Based on Redox-Chromophore Modified Nanostructured Semiconducting and Conducting Films. *J. Phys. Chem. B* **2000,** *104*, 11449-11459.
50. Brennaman, M. K.; Norris, M. R.; Gish, M. K.; Grumstrup, E. M.; Alibabaei, L.; Ashford, D. L.; Lapides, A. M.; Papanikolas, J. M.; Templeton, J. L.; Meyer, T. J., Ultrafast, Light-Induced Electron Transfer in a Perylene Diimide Chromophore-Donor Assembly on TiO_2. *J. Phys. Chem. Lett.* **2015,** *6*, 4736-4742.
51. Sampaio, R. N.; Piechota, E. J.; Troian-Gautier, L.; Maurer, A. B.; Hu, K.; Schauer, P. A.; Blair, A. D.; Berlinguette, C. P.; Meyer, G. J., Kinetics Teach that Electronic Coupling Lowers the Free-Energy Change that Accompanies Electron Transfer. *Proc. Natl. Acad. Sci. USA* **2018**, *115*, 7248-7253.
52. Hu, K.; Blair, A. D.; Piechota, E. J.; Schauer, P. A.; Sampaio, R. N.; Parlane, F. G. L.; Meyer, G. J.; Berlinguette, C. P., Kinetic Pathway for Interfacial Electron Transfer From a Semiconductor to a Molecule. *Nat. Chem.* **2016,** *8*, 853-859.
53. Hu, K.; Sampaio, R. N.; Marquard, S. L.; Brennaman, M. K.; Tamaki, Y.; Meyer, T. J.; Meyer, G. J., A High-Valent Metal-Oxo Species Produced by Photoinduced One-Electron, Two-Proton Transfer Reactivity. *Inorg. Chem.* **2018,** *57*, 486-494.
54. Williams, G.; Watts, D. C., Non-symmetrical dielectric relaxation behaviour arising from a simple empirical decay function. *Trans. Faraday Soc.* **1970,** *66*, 80-85.

For TOC use only